AGU PUBLICATIONS

JGR

Journal of Geophysical Research: Space Physics

RESEARCH ARTICLE
10.1002/2014JA020176

Key Points:
- Pitch angle distributions of electrons up to MeV at tailside are analyzed
- Changes in the numbers of observed cigar and isotropic events are connected
- Adiabatic accelerations can explain these changes over a large range of energy

Supporting Information:
- Readme
- Table S1

Correspondence to:
K. Wang,
ktwang@pssc.ncku.edu.tw

Citation:
Wang, K., C.-H. Lin, L.-Y. Wang, T. Hada, Y. Nishimura, D. L. Turner, and V. Angelopoulos (2014), Pitch angle distributions of electrons at dipolarization sites during geomagnetic activity: THEMIS observations, *J. Geophys. Res. Space Physics*, *119*, 9747–9760, doi:10.1002/2014JA020176.

Received 13 MAY 2014
Accepted 11 NOV 2014
Accepted article online 15 NOV 2014
Published online 9 DEC 2014

Pitch angle distributions of electrons at dipolarization sites during geomagnetic activity: THEMIS observations

Kaiti Wang[1], Ching-Huei Lin[2], Lu-Yin Wang[3,4], Tohru Hada[5,6], Yukitoshi Nishimura[7], Drew L. Turner[8], and Vassilis Angelopoulos[8]

[1]Institute of Space and Plasma Sciences, National Cheng Kung University, Tainan, Taiwan, [2]Department of Electrical Engineering, Chien-Hsin University of Science and Technology, Jung-Li, Taiwan, [3]Department of Physics, National Cheng Kung University, Tainan, Taiwan, [4]Department of Aerospace Engineering, University of Michigan, Ann Arbor, Michigan, USA, [5]Interdisciplinary Graduate School of Engineering Sciences, Kyushu University, Kasuga, Japan, [6]International Center for Space Weather Science and Education, Kyushu University, Fukuoka, Japan, [7]Department of Atmospheric and Oceanic Sciences, University of California, Los Angeles, California, USA, [8]Department of Earth, Planetary, and Space Sciences, University of California, Los Angeles, California, USA

Abstract Changes in pitch angle distributions of electrons with energies from a few eV to 1 MeV at dipolarization sites in Earth's magnetotail are investigated statistically to determine the extent to which adiabatic acceleration may contribute to these changes. Forty-two dipolarization events from 2008 and 2009 observed by Time History of Events and Macroscale Interactions during Substorms probes covering the inner plasma sheet from 8 R_E to 12 R_E during geomagnetic activity identified by the *AL* index are analyzed. The number of observed events with cigar-type distributions (peaks at 0° and 180°) decreases sharply below 1 keV after dipolarization because in many of these events, electron distributions became more isotropized. From above 1 keV to a few tens of keV, however, the observed number of cigar-type events increases after dipolarization and the number of isotropic events decreases. These changes can be related to the ineffectiveness of Fermi acceleration below 1 keV (at those energies, dipolarization time becomes comparable to electron bounce time). Model-calculated pitch angle distributions after dipolarization with the effect of betatron and Fermi acceleration tested indicate that these adiabatic acceleration mechanisms can explain the observed patterns of event number changes over a large range of energies for cigar events and isotropic events. Other factors still need to be considered to assess the observed increase in cigar events around 2 keV. Indeed, preferential directional increase/loss of electron fluxes, which may contribute to the formation of cigar events, was observed. Nonadiabatic processes to accelerate electrons in a parallel direction may also be important for future study.

1. Introduction

During dipolarization, which has been observed at Earth's tailside during geomagnetic activity [*Baumjohann et al.*, 1999], several features associated with electron distributions have been detected, including particle injections and variations in pitch angle distributions. Rapid energization of electrons (injections) under magnetic field dipolarization appears to be common from geosynchronous altitude to 30 R_E [*Gabrielse et al.*, 2014], and injection properties and associated with ion injection, flow, and magnetic field variations depend critically on the satellite's location relative to the dipolarizing flux bundles and associated flow bursts. Several observed injection features have also been reproduced in a test particle approach in which spatial properties of injection regions and anisotropy of electrons were investigated [*Birn et al.*, 2014].

Some electron pitch angle distribution (PAD) studies have included the nightside tail region [e.g., *West et al.*, 1973; *Smets et al.*, 1999; *Sergeev et al.*, 2001; *Shiokawa et al.*, 2003; *Åsnes et al.*, 2005; *Wu et al.*, 2006; *Wang et al.*, 2010; *Fu et al.*, 2011, 2012b; *Runov et al.*, 2013]. Among these, *Smets et al.* [1999], *Wu et al.* [2006], *Fu et al.* [2012b], and *Runov et al.* [2013] reported variations in pitch angle distributions observed at dipolarization sites.

Smets et al. [1999] studied 10 keV electron pitch angle distributions as a function of spatial location along the tail region after the dipolarization phase of a substorm. They reported Interball observations of PADs at

various locations and explained them in the framework of Fermi and betatron acceleration at different locations along the tail. The pitch angle distributions were found to be perpendicular peaked (i.e., pancake), ring-type (i.e., butterfly), and beamlike at $L = 7$, 9, and 11, respectively. The ring-type distributions were explained as a result of the transition region between dipole and tail-like configuration. The pancake and beamlike distributions were explained from variations of relative importance between betatron and Fermi accelerations at dipole and tail-like configuration regions.

Wu et al. [2006] used Cluster observations to study the evolution of energetic (20–200 keV) electron pitch angle distributions in the midtail ($>10\ R_E$) that accompanied substorm-associated magnetic field dipolarizations. Electron fluxes were observed to increase for perpendicular pitch angles (pancake distribution), which evolved into isotropic distributions, then evolved into mixed distributions, a combination of perpendicularly peaked distributions and beamlike distributions. At the end of each of three episodes, all PAD distributions evolved into a beamlike or field-aligned distribution. These phenomena have also been explained by a model based on betatron and Fermi accelerations in the study.

Fu et al. [2012b] adopted data of Cluster 1 to statistically examine the PAD of suprathermal electrons ($>$40 keV) inside the flux pileup regions (FPRs) behind the earthward propagating dipolarization fronts around $X_{GSM} < \sim -11\ R_E$ at tailside. Based on the anisotropy defined from the ratio of observed perpendicular and parallel flux, the pancake distribution is found to be primarily inside the growing FPR, the cigar distribution is mainly inside the decaying FPR, and the isotropic distribution is within the steady FPR. The mechanism of betatron cooling was specifically discussed, which also causes field-aligned acceleration as Fermi acceleration does.

Runov et al. [2013] used Time History of Events and Macroscale Interactions during Substorms (THEMIS) observations to investigate the PAD of low-energy (0.2 keV) electrons and omnidirectional energy-time spectrograms of higher-energy (30–500 keV) electrons observed at and near dipolarization fronts in the plasma sheet. In the three cases investigated, pancake-type and cigar-type distributions were found to coexist at the same front. The results suggest that energetic electron PADs are mainly pancake type near the neutral sheet ($|B_x| < 10$ nT) and mainly cigar type above and below it ($|B_x| > 10$ nT). The betatron effect was remarked to be related to a short dropout in the energetic electron fluxes.

The above case studies of electron PAD focused mainly on limited energy. However, because changes in electron pitch angle distributions would not be confined to a limited energy range during dipolarization, it would be beneficial to acquire a statistical picture of these changes versus energies at a large range. The significance of adiabatic acceleration mechanisms (betatron and Fermi accelerations) to these electron PAD changes at different energies during the dipolarization process can thus also be examined. Since the THEMIS mission covers a wide range of radial distances around the equatorial plane in Earth's magnetotail, and electron energies from a few eV up to 1 MeV can be detected, we use its observational data set to investigate variations in pitch angle distributions of electrons at different energy channels at dipolarization sites.

2. Instruments and Data Analysis

The THEMIS (Time History of Events and Macroscale Interactions during Substorms) mission, launched in 2007, was designed to address substorm-related questions using coordinated multipoint observations [e.g., *Angelopoulos et al*., 2008]. Its five probes (THA, THB, THC, THD, and THE) carry identical instruments to measure plasma parameters. Although the probes' highly eccentric orbits near the equatorial plane cover wide radial distances, most sampling is done from about 8 R_E to 30 R_E.

The charged particle instruments on THEMIS are the electrostatic analyzer (ESA) and the solid state telescope (SST). The ESA measures electrons and ions from 3 eV to 30 keV; the SST measures electrons from 30 keV to 6 MeV. The full distributions for particle fluxes of different energies from all incoming directions can be detected within 32 spins (~96 s), so pitch angle distributions of charged particles can be determined every 96 s. Electron data from all ESA and SST energy channels (30 ESA channels and 10 SST channels) were analyzed. Pitch angle distributions were derived from the THEMIS Data Analysis Software provided by the mission.

Dipolarization events observed when probe apogees were located on the tailside of the geomagnetic field system were selected for this study. To enhance our understanding of the effect of dipolarization on electron

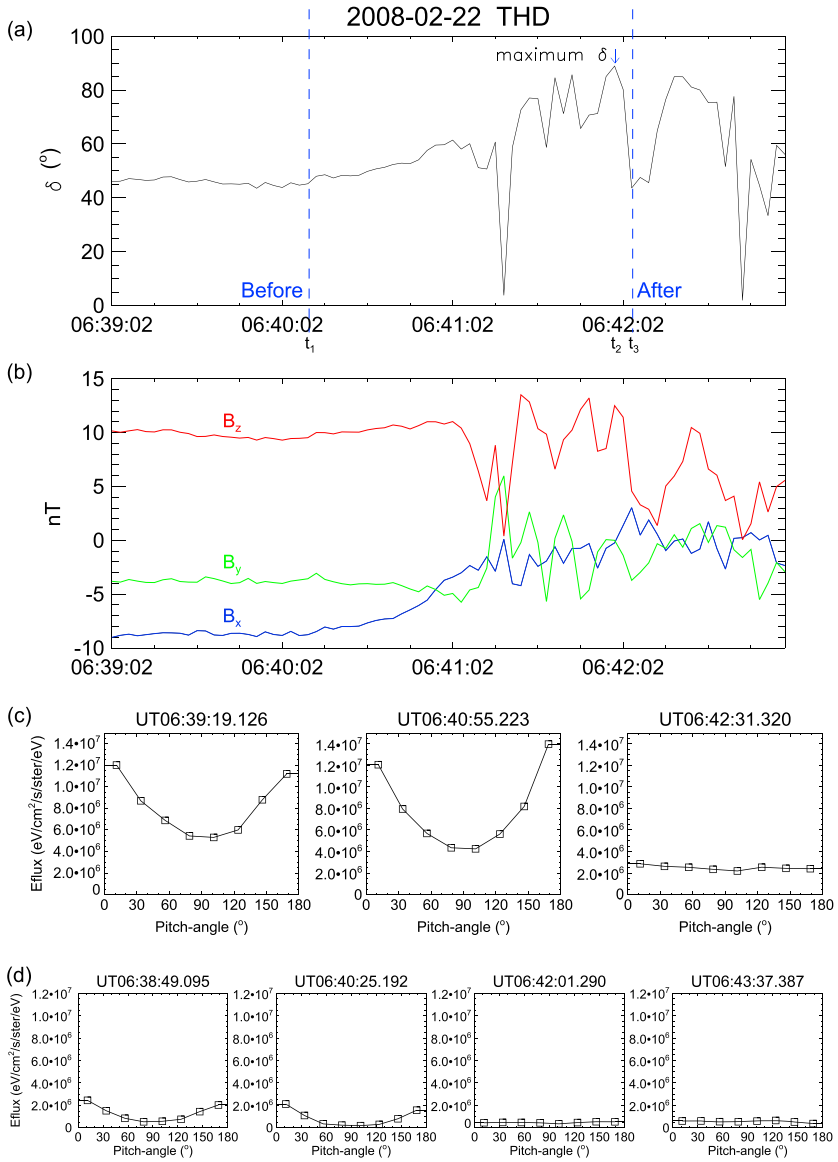

Figure 1. (a) The dipolarization angle δ derived from FGM magnetic field data for 22 February 2008 event observed by THD. Time is plotted from 06:39:02 to 06:43:00 UT (x axis). The blue lines demarcate the time of this variation. The blue arrow indicates when the maximum δ occurred. (b) The three magnetic field components B_x, B_y, and B_z from FGM measurements. (c) The corresponding PAD in time sequence (left to right) observed by ESA at the highest-energy channel (20,026 eV). (d) The corresponding PAD in time sequence (left to right) observed by SST at the lowest-energy channel (29800 eV).

distribution, we selected events that were not limited to be associated with aurora observations. Instead, because many dipolarization events found in the 2008 to 2009 THEMIS data occurred as *AL* index values became more negative, these events were selected. Dipolarization events that occurred as the *AL* index recovered from its minimum were excluded to ensure that those selected for our database occurred during periods with similar geomagnetic disturbances. To select appropriate events for analysis, the dipolarization angle δ, defined as $\tan^{-1}(B_z/(B_x^2+B_y^2)^{1/2})$, where B_x, B_y, and B_z are the measured magnetic field components in the GSM coordinate system, is examined. Figure 1 shows an example of dipolarization. Magnetic field data measured by the THEMIS fluxgate magnetometer (FGM) (Figure 1b) are adopted to calculate the temporal change in δ (Figure 1a) [*Auster et al.*, 2008]. This case is from 22 February 2008, when the *AL* index was decreasing to −340 and THD was located at $X_{GSM} = -11.31$, $Y_{GSM} = 1.92$, and $Z_{GSM} = -2.74$. The angle δ was near 45° before 06:40:11 UT (t_1), marked by the first blue dashed line. Subsequently, it maintained mostly large values with some fluctuations and rose to maximum of about 90° at 06:41:59 UT (t_2) as the blue arrow

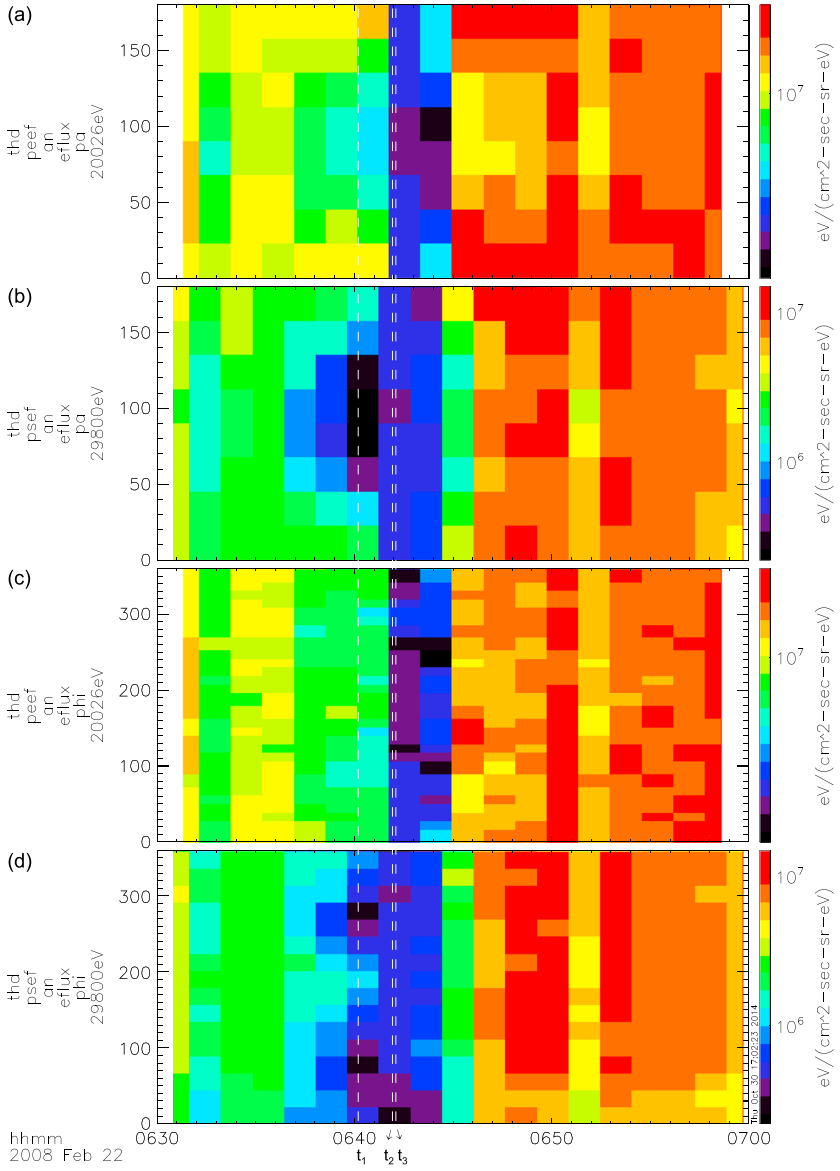

Figure 2. Angular spectrum (y axis) versus time (x axis) of the observed differential energy flux of electrons based on the dipolarization event in Figure 1. (a) Spectrum in the pitch angle α for the highest-ESA-energy channel (20,026 eV). (b) Spectrum in the pitch angle α for the lowest-SST-energy channel (29,800 eV). (c) Spectrum in the azimuthal angle Φ for the highest-ESA-energy channel (20,026 eV). (d) Spectrum in the azimuthal angle Φ for the lowest-SST-energy channel (29,800 eV). The vertical white dashed lines indicate the time at t_1, t_2, and t_3 as shown in Figure 1a.

indicates. After t_2, δ dropped back to about 45° at 06:42:05 UT (t_3). After this time t_3 (represented by the other blue dashed line), the field again became less dipolarized. In this plot (Figure 1a), the time before t_1 is denoted as "before" dipolarization, and the time after t_3 is denoted as "after" dipolarization. Therefore, the pitch angle distributions before dipolarization were determined from data recorded at the time before and closest to t_1, which would be within the temporal resolution of the data, 96 s, and those after dipolarization were determined from data recorded after and closest to t_3, also within 96 s. Although, as shown in Figure 1a, other dipolarizations occurred after t_3, only the first dipolarization event was selected. In this study, the dipolarization time for each event was determined based on the criteria shown in this example. In addition, (1) only events with probe positions within 45° of the X_{GSM} axis were selected to exclude those that occurred at the low-latitude boundary layer. (2) Only events that occurred in the region with plasma $\beta > 0.5$ (thought to be the inner plasma sheet [*Angelopoulos et al.*, 1994; *Grigorenko et al.*, 2012])

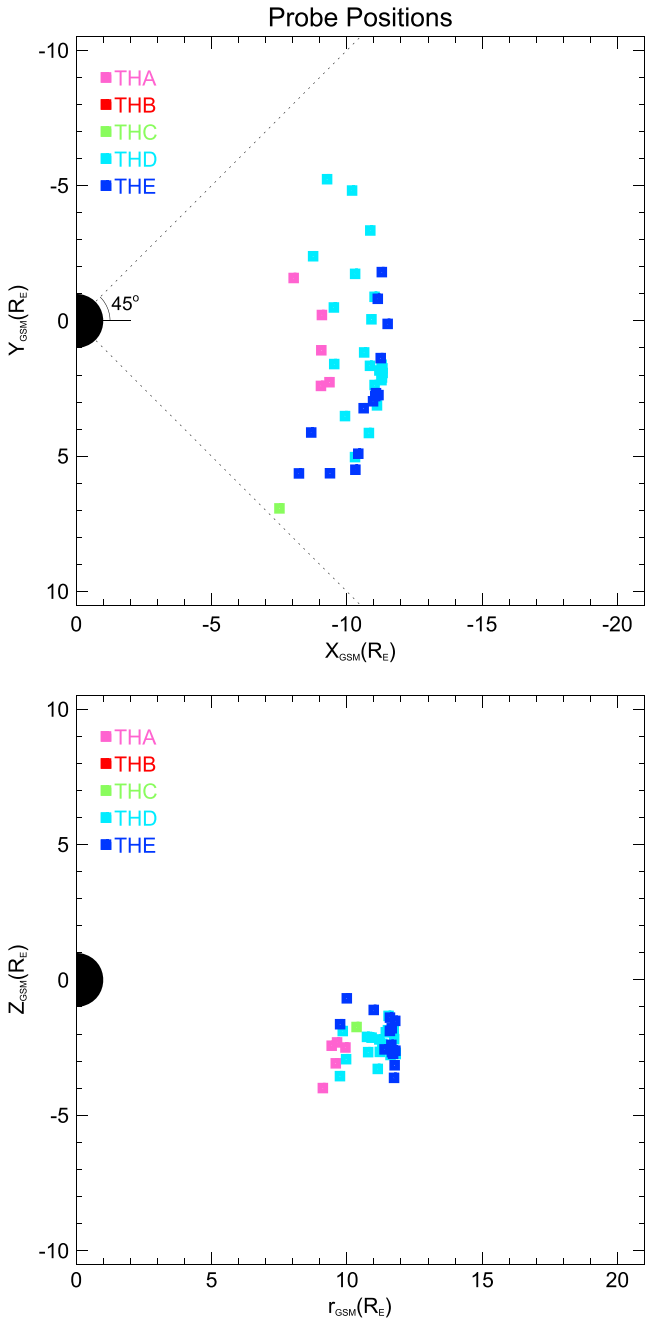

Figure 3. (top) THEMIS probe positions for 42 selected events in the inner plasma sheet in the *x-y* plane in GSM coordinates. (bottom) Probe positions for the selected events in the *r-z* plane in GSM coordinates.

before and after dipolarization were taken into account. (3) Events caused by flapping of the magnetotail were excluded. (4) Events with dipolarization-like behavior but related to plasma sheet boundary crossings were excluded. (5) Events with no significant change in dipolarization angle δ were also excluded. That is, all δ in the event database with a change more than 15° became greater than 20° and increased by more than a factor of 1.5 after dipolarization, satisfying the criteria adopted by *Sigsbee et al.* [2005].

Observed variations of PADs at dipolarization for this event are shown in Figures 1c and 1d. Figure 1c shows the observed temporal changes for the highest-energy channel of ESA at 20026 eV (Figure 1c, left to right). The observed differential energy flux (marked as eflux in the plots) of electrons versus pitch angles is plotted. The default data set provided by the THEMIS mission is gridded by eight cones from pitch angle $\alpha = 0°$ to 180°; each cone is 22.5° wide. The eight halo squares in each panel of Figures 1c and 1d present the eight data values of each cone. After dipolarization, the PAD evolved from cigar distributions (peak at $\alpha = 0°$, 180°) to isotropic distributions, and the total flux decreased (Figures 1c and 1d, left to right). Figure 1d shows the temporal changes for the lowest-energy channel of SST at 29,800 eV; evolution from cigar distributions to more isotropic distributions (Figure 1d, left to right) is also shown. The observed angular distributions of electron fluxes of longer period at the ESA's highest-energy channel and the SST's lowest-energy channel for each dipolarization event are examined to ensure that only events with consistently observed features across these interface channels are selected for the event database. Figure 2 illustrates this examination for the event in Figure 1 shown from 06:30 UT to 07:00 UT. Figures 2a and 2b show the pitch angle distributions of differential energy flux observed in this period; they feature with decrease from 06:30 to 06:40 UT and then gradually increase with time. In observations of the highest-ESA channel (Figure 2a) and the lowest-SST channel (Figure 2b) from 06:37 UT, the PAD exhibits a cigar-type distribution before t_1 and becomes more isotropic with increasing time after t_3. Figures 2c and 2d are spectrograms of the observed differential energy flux of electrons versus Φ. (The azimuthal angle, Φ, is the angle relative to the probe-Sun direction in the probe's spin plane.) Figure 2c shows the highest-energy-ESA channel, and Figure 2d shows the lowest-SST channel. Both figures also indicate that

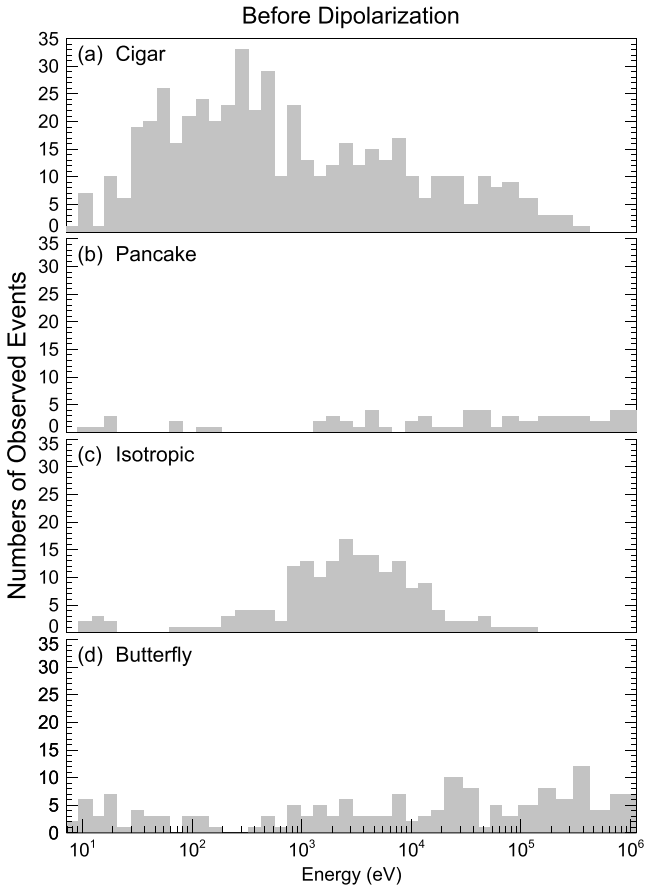

Figure 4. (a–d) Number of observed events versus all energy channels before dipolarization for the four types of pitch angle distributions in this study. Types of PAD are shown in each panel from Figures 4a–4d.

the differential energy flux in all Φ decreases from 06:30 to 06:40 UT and then gradually increases with increasing time. Hence, the observed features in both PAD and Φ crossing the energy channels of ESA and SST are examined to be consistent, so this event is selected in the event base. Sun contamination has been removed from the SST data. After implementing the above steps, 42 dipolarization events from 4 February to 13 March 2008 and from 1 February to 15 March 2009 were selected. Table S1 in the supporting information displays the observed dipolarization starting time and the THEMIS probe associated with each event. The event in Figure 1 corresponds to event no. 13 in this table. Figure 3 shows the probe positions (marked in different colors) during these 42 events. Figure 3 (top) shows the probe positions in the *x-y* plane, and Figure 3 (bottom) shows them in the *r-z* plane, both in GSM coordinates. The observed pitch angle distributions of electrons from these events were analyzed. In addition to the cigar and isotropic distributions shown in Figures 1c and 1d, four other major types of pitch angle distributions were also found in the data. These include pancake (peak at 90°), butterfly (peaks between both 0° and 90°, and 90° and 180°), combo (peaks at 0°, 90°, and 180°), and beam distributions (peaks in a specific angle with other angles dropping to below detectable thresholds). Beam distributions were only found for electrons with energies exceeding 60 keV. The remainder of the PADs usually exhibit a peak at one specific angle (except 90°) and gradually decrease at other angles. Others may exhibit a peak only at 0° or 180°, probably due to electron loss to the atmosphere within a bounce period. Some other distributions have two or more peaks at other pitch angles. These cannot be categorized as any of the above types. They are probably transition states of pitch angle evolution as electrons gyrate and bounce along field lines as the field strength/configuration changes during dipolarizations.

To pursue the effect of betatron and Fermi accelerations on PAD of electrons when dipolarization occurs, cigar, pancake, isotropic, and butterfly distribution events are investigated. If the electron PADs are isotropic before dipolarization, the dominance of Fermi acceleration could account for their cigar distribution after dipolarization. The dominance of betatron acceleration, however, could account for their pancake distribution after dipolarization. The butterfly distributions may be transitory, eventually evolving into cigar or pancake distributions. For the above reasons, these four types of PAD events are further investigated. The types of PAD have been attributed to preferential peaks of distributions in specific pitch angles. Since the isotropic distribution has been inferred to have no significant peak in any direction [e.g., *Wu et al*., 2006] but have given no specific quantitative definition, we define isotropic events using an additional criterion: the percentage differences of the observed differential energy flux between cones must not exceed 25%. In Figure 1c (right), the value of this percentage difference is 23.31%, so this event is categorized as isotropic after dipolarization. Nevertheless, in Figure 1d, although the PAD is isotropized after dipolarization, since the percentage difference is 41.72% (Figure 1d, right), the PAD after dipolarization is not included in the database

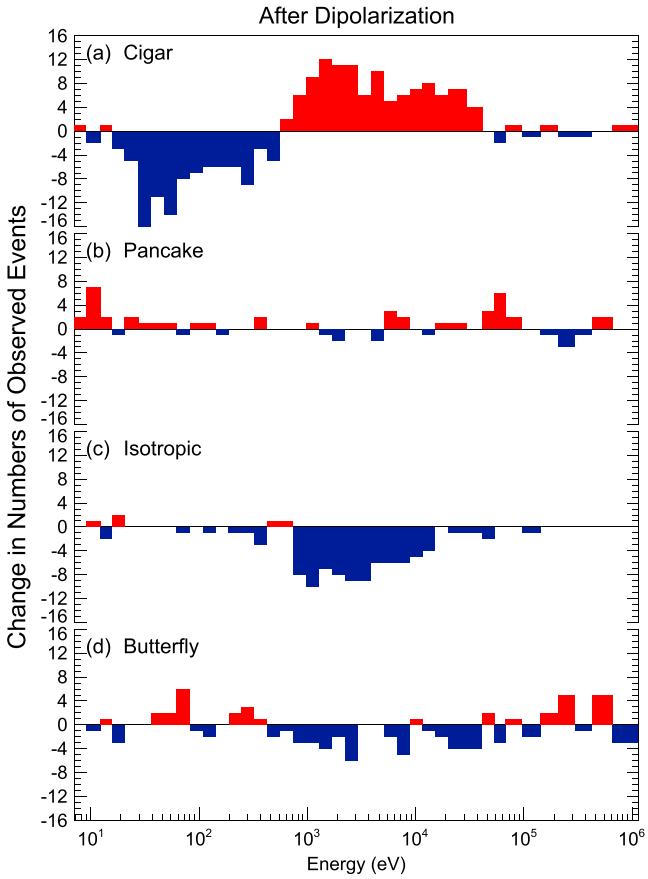

Figure 5. (a–d) Variations in the number of observed events versus all energy channels after dipolarization for different types of pitch angle distribution. Types of PAD are shown in each panel from Figures 5a–5d. The red bars indicate the increased numbers, and the blue bars indicate the decreased numbers.

as an isotropic event. Figure 4 is a histogram of the numbers of observed events (42 in Table S1 in the supporting information) versus energies for the four types of PAD before dipolarization. The number of cigar events, the largest among these four types of PAD events, peaks at the energy channel around 300 eV (Figure 4a). The number of isotropic events is the second largest with peak number at 3 keV (Figure 4c). There are more butterfly events (Figure 4d) than pancake events (Figure 4b). Both pancake and butterfly events occur more often at higher-energy channels than at lower energy channels.

Figure 5 shows the histograms of changes in the numbers of observed events for the four types of PAD after dipolarization versus different energy channels. The number of cigar distribution events decreases at energy levels below about 1 keV after dipolarization (Figure 5a). If effective betatron acceleration had taken place during dipolarization, these cigar events would have become more isotropic. As shown in Figures 5a and 5c, at similar energy levels, the numbers of cigar events above 1 keV increase, whereas those for isotropic events decrease, suggesting that Fermi acceleration may become effective at these energy levels. When the evolution of observed PADs was analyzed event by event, numerous events were found to start with cigar distributions and end with more isotropic distributions at a few hundreds of eV levels. Many of them, however, did not reach the quantitative criteria to be categorized as isotropic events so the change in numbers below 1 keV in Figure 5c is limited. Also, many events that began with isotropic distributions ended with cigar distributions after dipolarization at an energy level above 1 keV. Therefore, as shown in Figures 5a and 5c, the changes in the numbers of observed cigar events and isotropic events tend to exhibit opposite phases over energies above 1 keV to 50 keV. After dipolarization, there are noticeable increases in pancake event numbers around 10 eV and 60 keV (Figure 5b). Before dipolarization, butterfly event numbers peak at ~20 keV and a few hundreds of keV (Figure 4d). After dipolarization, these numbers increase even more at above 200 keV and below 1 keV yet decrease in the energy level in between (Figure 5d).

3. Conservation of the First and Second Adiabatic Invariants

To discuss the features of change in the numbers of observed events for the four types of PAD in Figure 5 more systematically, betatron and Fermi accelerations are considered. The goal is to enhance our understanding of the extent to which these adiabatic acceleration processes can account for the observations. The fundamental concept is to input the observed PAD before dipolarization, through calculations of changes in pitch angles based on betatron and Fermi accelerations, to acquire the PAD after dipolarization. Because field lines in the inner plasma sheet are closed, the effects of conservation of first and second adiabatic invariants can be considered toward betatron and Fermi accelerations.

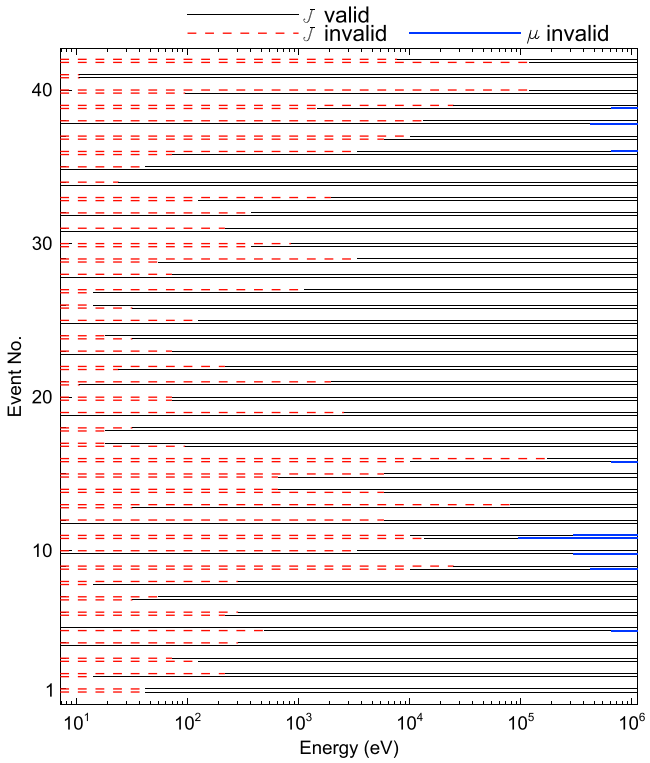

Figure 6. Validity of the second adiabatic invariant *J* for each event. The *y* axis shows the event number based on Table S1 in the supporting information. For each event, there are two corresponding horizontal lines. The bottom one shows the validity from the beginning of dipolarization (t_1) to the time when δ reaches maximum (t_2), and the top one shows the validity from the time of maximum δ (t_2) to the end of dipolarization (t_3). The red dashed lines represent the energy range over which *J* is not valid; the solid lines indicate the valid energy range. The blue lines represent the energy channels in which the first adiabatic invariant μ becomes invalid due to the large Larmor radius.

Before applying these invariants to obtain the magnitudes of acceleration/deceleration in the perpendicular and parallel directions, the validity of their invariance needs to be checked thoroughly for each energy channel for each event. This depends on both the temporal and spatial scales of the dipolarization. For the first adiabatic invariant μ to be valid, the time scale of the gyroperiod τ_g must be smaller than the dipolarization time ($\varepsilon_t = |\tau_g \partial_t (\ln B)| \ll 1$). For the second adiabatic invariant *J* to be valid, the bounce period τ_b must satisfy $\varepsilon_t = |\tau_b \partial t (\ln B)| \ll 1$. In addition, the Larmor radius ρ must be smaller than the spatial scale of varying magnetic fields to satisfy $\varepsilon_r = \max|\rho \nabla_\perp (\ln B), \rho \nabla_{||} \hat{b}| \ll 1$, and $\varepsilon \leqq 0.187$ is selected [*Elkington et al.*, 2002]. The critical value ε is determined from the criteria that the perturbation above which the adiabatic motion will be violated satisfies $e^{-1/\varepsilon} = \varepsilon/4\pi^2$ [*Chirikov*, 1987]. The validity of these invariants is examined from the observed ambient magnetic field strengths B_1, B_2, and B_3 and the probe location in *L* shells L_1, L_2, and L_3 at t_1, t_2, and t_3 for each event. Here the field-line length is considered to be proportional to *L*. For convenience, a dipole field configuration is chosen: τ_g and τ_b are modeled based on a dipole with relativistic effects taken into account [*Walt*, 2005]. As the *L* shell increases, the field line is more stretched so τ_b from a dipole actually represents the minimum bounce period. The actual bounce period, which can be even closer to the dipolarization time, results in more cases that violate the second adiabatic invariants. The spatial scale parallel to the field line is chosen to be from the equator to the latitude where the field strength is doubled, so it is the field-line length from the magnetic equator to magnetic latitude 24°. As to the spatial scale perpendicular to the field line, the criterion $\varepsilon = \rho|\nabla_\perp (\ln B)| \leqq 0.187$ indicates that ρ needs to be smaller than 0.0623 *L* to allow the μ conservation to be valid.

The observed dipolarization time for these events ranges from a few tens to hundreds of seconds. This time period is divided into two parts and compared with τ_g and τ_b (from t_1 to t_2 and from t_2 to t_3 (refers to Figure 1a)). The validity of the second adiabatic invariant *J* for the observed events based on the criteria above is shown in Figure 6. The *y* axis gives the event number based on Table S1 in the supporting information; the *x* axis shows the energy channels. There are two lines for each event: The bottom line represents the validity from t_1 to t_2; the top line represents the validity from t_2 to t_3. The red dashed part represents the energy range for which the second adiabatic invariant *J* is invalid; the solid black part denotes the range for which it is valid. The plot shows that for most events, the second adiabatic invariant is invalid for electrons below 1 keV. Thus, we expect that the Fermi acceleration is not operational for electrons below 1 keV during dipolarization. The blue parts at high energy levels for some events represent the energy channels for which even the first adiabatic invariant μ is invalid because of the large ρ of electrons at this high energy level.

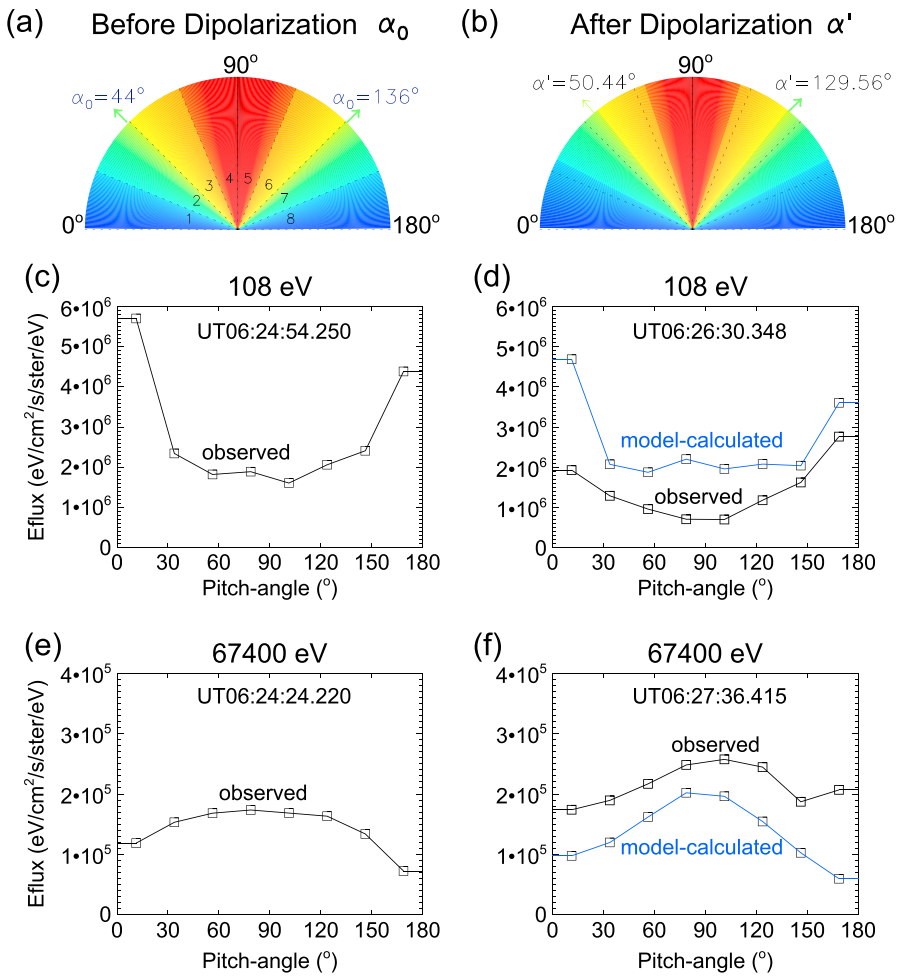

Figure 7. Modeled variations of the pitch angles of electrons and PAD types for the dipolarization event detected by THD at around 06:25 UT on 22 February 2008. (a) The uniformly distributed initial α (α_0) in eight cones (denoted by 1, 2, 3… 8) from 0° to 180° with a size of 22.5° of each cone. The different colors present various α_0. (b) The model-calculated α after dipolarization (α') from the conservation of the adiabatic invariants. The α becomes perpendicular as the light green arrow indicates. (c) The observed PAD of electrons before dipolarization at the 108 eV energy channel. (d) The model-calculated PAD after dipolarization (blue line) based on the variation of α shown in Figures 7a and 7b. The observed PAD after dipolarization is plotted as a solid black line. (e) The observed PAD of electrons before dipolarization at the 67,400 eV energy channel. (f) The model-calculated PAD based on the variation of α in Figures 7a and 7b for 67,400 eV. The observed PAD after dipolarization at this energy channel is also plotted as a solid black line.

The next step is to calculate the pitch angle α after dipolarization. Here the phase space density (PSD) is assumed to be constant, and the probes observed the same population during dipolarization. This implies that the flux tubes initially have the same PSD, and they are pushed around by the dipolarization but retain the memory of having come from that PSD. Therefore, for an electron with initial pitch angle $\alpha_0 = \tan^{-1}(V_{\perp 1}/V_{\parallel 1})$, perpendicular velocity $V_{\perp 1}$, and parallel velocity $V_{\parallel 1}$, if μ is valid from t_1 to t_3, the ratio between its perpendicular velocity $V_{\perp 3}$ and $V_{\perp 1}$ is $(B_3/B_1)^{1/2}$. As shown in Figure 6, there are energy channels for which μ are invalid. Therefore, if μ is valid from t_1 to t_2 but invalid from t_2 to t_3, $V_{\perp 3}/V_{\perp 1}$ is assumed to be $V_{\perp 2}/V_{\perp 1} = (B_2/B_1)^{1/2}$; if μ is invalid from t_1 to t_2 but valid from t_2 to t_3, then $V_{\perp 3}/V_{\perp 1}$ is assumed to be $V_{\perp 3}/V_{\perp 2} = (B_3/B_2)^{1/2}$. When μ is invalid, the electrons are not confined by the magnetic fields and may become more isotropic unless there are large changes in magnetic field strengths later. The detail changes in angular distributions require particle simulation through case studies. Figure 6 shows that this violation of μ took place at higher-energy channels for only a few events (blue parts), so here this isotropization is not elaborated. If the second adiabatic invariant J is valid from t_1 to t_3 because the field-line length is proportional to the L value, we have $V_{\parallel 3}/V_{\parallel 1} = (L_1/L_3)$. If it is valid from t_1 to t_2 but invalid from t_2 to t_3, the change in parallel velocity is not

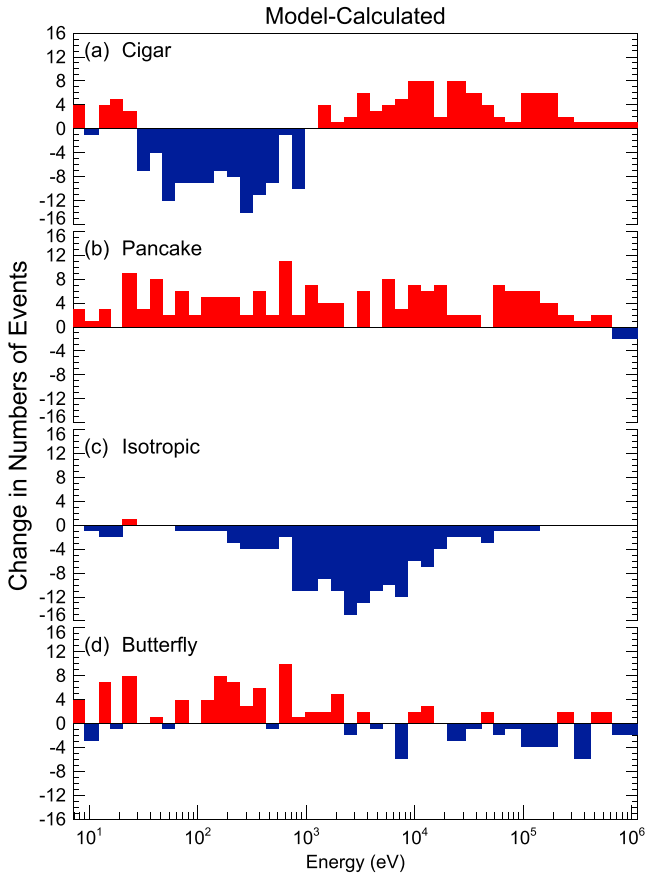

Figure 8. The model-calculated change in event number versus all energy channels after dipolarization for the four types of pitch angle distributions at different regions. (a–d) The cigar, pancake, isotropic, and butterfly distribution events.

taken into account from t_2 to t_3 in the current calculation, and $V_{\parallel 3}/V_{\parallel 1}$ is assumed to be (L_1/L_2). If J is invalid from t_1 to t_2 and from t_2 to t_3, the change in $V_\parallel$ is not considered, so $V_{\parallel 3}$ is assumed to be $V_{\parallel 1}$. Again, using the observed magnetic field strengths B_1, B_2, and B_3 and the probe position in the L shell as L_1, L_2, and L_3, based on a dipole, the above calculation can be carried out. After dipolarization, the electron pitch angle α becomes $\tan^{-1}(V_{\perp 3}/V_{\parallel 3})$.

The above information on pitch angle changes during dipolarization for each energy channel of each event can be used to calculate the evolved PAD after dipolarization, based on the observed PAD before dipolarization. The method is illustrated in Figure 7. Figure 7a exhibits the eight equally divided cones in pitch angles from 0° to 180° marked from 1 to 8. The different colors represent the electrons with different initial pitch angles α_0 before dipolarization. The colors have been plotted to be blue based in cones 1 and 8, light blue/light green in cones 2 and 7, yellow based in cones 3 and 6, and red based in cones 4 and 5. The event observed at 06:25 UT on 22 February 2008 by the THD is the example (i.e., event no. 12 in Table S1 in the supporting information) for this illustration. The pitch angle after dipolarization, denoted as α' for each given α_0, can be derived from the observed B_1, B_2, B_3, L_1, L_2, and L_3 from the steps depicted in the previous paragraph. From Figure 6, J is only valid above 60 keV for this event for the entire dipolarization process (i.e., event no. 12, solid black line). However, since the L value of the probe for this event does not change, only betatron acceleration is effective. As shown in Figure 7b, the calculated electron pitch angles move toward the perpendicular direction after this dipolarization. For example, electrons with $\alpha_0 = 44°$ and 136° (light green arrow in Figure 7a) change their pitch angles to $\alpha' = 50.44°$ and 129.56°, respectively (light green arrow in Figure 7b). Consequently, after dipolarization, these pitch angles move from the second cone into the third cone and from the seventh cone into sixth cone. Figure 7b also shows that some electron populations with α_0 originally in the first and eighth cones (blue-based colors in Figure 7a) move into the second and seventh cones, respectively, as shown by the blue-based colors in Figure 7b; after dipolarization, some of those in the third and sixth cones (yellow-based colors in Figure 7a) move into the fourth and fifth cones, respectively, as shown by the yellow-based colors in Figure 7b. Hence, the portion of the measured differential energy flux of electrons in a given cone that transferred to another cone because of changes in their pitch angles can be acquired based on the information on changes from α_0 to α' when dipolarization occurs. The PAD after dipolarization can then be calculated. Figure 7c shows the PAD of electrons observed by ESA in the 108 eV energy channel before dipolarization for this event. Figure 7d exhibits the model-calculated PAD from this observed PAD, with drops at both 0° and 180° but increases at around 90°. The observed PAD after dipolarization is in cigar distributions (solid black line), with distinct drops at both 0° and 180°. Figure 7e shows the observed PAD before dipolarization at a higher-energy channel (67,400 eV) measured by SST, which peaks around 90°, and so is categorized as pancake distribution. The model-calculated PAD shows a sharper pancake distribution, a consequence of pitch

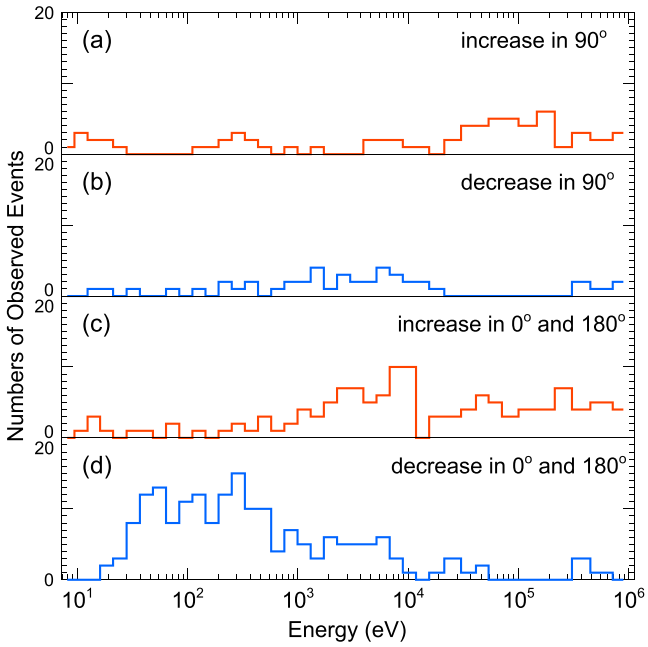

Figure 9. Number of observed events with dominant directional flux changes after dipolarizations at specific pitch angles versus energies. (a) Preferential 90° increase, (b) 90° decrease, (c) 0° and 180° increases, and (d) 0° and 180° decreases.

angles moving toward 90° (Figure 7f). The observed PAD (solid black line) at this energy channel also shows a sharper pancake-like distribution. In practice, since the electron energies could change to other energy channels when their pitch angles change after dipolarization, such electron populations are also added or subtracted to finalize the model-calculated PAD. These final model-calculated PADs are categorized using the same criteria adopted in Figures 4 and 5. The change in the numbers of events using the final model-calculated PAD as the PAD after dipolarization is shown in Figure 8. The calculated numbers of cigar events after dipolarization exhibit a decrease at energy levels below about 1 keV (Figure 8a) (note that the Fermi acceleration is not effective under this energy level (Figure 6)). The model-calculated numbers of cigar events above 1 keV increase with a peak value of +8 events around 10 keV (Figure 8a); the observed change in the numbers of cigar events has an even more distinct increase with a peak value of +12 events around 2 keV. A pattern over energies resembling the observations shown in Figure 5a is exhibited: Decrease in lower energy channels below 1 keV (blue colored) and increase at higher energy levels above 1 keV (red colored), except for above 60 keV, of which the model-calculated results show an excess number increase compared with the numbers above this energy level in Figure 5a.

Although the patterns of this change in the numbers of events over energies are similar, the model-calculated results show less increase, (especially between ~1 keV and 10 keV) than observed results (Figures 8a and 5a). Nonadiabatic mechanisms could cause parallel acceleration, such as accelerated from external electric fields or from pitch angle scattering by whistler mode waves. Flux loss in $\alpha = 90°$ could also be important [e.g., *Hada et al.*, 1981; *Asano et al.*, 2010]. Such electric fields have been observed at dipolarization fronts [*Apatenkov et al.*, 2007; *Runov et al.*, 2011; *Gabrielse et al.*, 2012; *Fu et al.*, 2012a; *Huang et al.*, 2012a] and whistler mode waves during dipolarizations [*Le Contel et al.*, 2009; *Deng et al.*, 2010; *Huang et al.*, 2012a]. The factors can also be external sources of electron population, such as an ionospheric source of field-aligned moving electrons [*Hada et al.*, 1981; *Abel et al.*, 2002]. Recently *Zheng et al.* [2012] reported Cluster observations of 1 keV electrons at the plasma sheet streaming from the ionosphere. This could supply more parallel-moving electrons at this energy level and produce more cigar events. Note that field lines at outer L shells in the tail (from 9 R_E to 19 R_E) have been observed to possess more cigar distributions [*Shiokawa et al.*, 2003]. Because field-line lengths will be shortened and may move closer to the Earth during dipolarization, probes may also detect electron populations associated with field lines from outer L shells, and the numbers of observed cigar events can rise. Figure 9 shows the analyzed numbers of observed events with flux changes in preferential directions after dipolarization versus energy channels based on events with significant increase/decrease in total flux. These numbers imply that when dipolarization occurs, external source/loss of flux is involved. Events with loss dominated in $\alpha = 90°$ as well as events with increases dominated in both 0° and 180° between 1 keV to 10 keV exist (Figures 9b and 9c). The increase in the numbers of cigar events above 1 keV may also be due to these preferential directional flux changes. Figure 9d also shows that decreases below 1 keV can be dominant in both 0° and 180°. This dominance can be caused by electrons with pitch angles inside the loss cone being ripped off into the atmosphere, which can also reduce the numbers of cigar events after dipolarization in addition to the ineffectiveness of Fermi acceleration at this energy level.

Furthermore, for the model-calculated pancake distribution events, the calculation produces an enhancement in numbers of events after dipolarization for most energy channels (Figure 8b). Because Fermi acceleration is not effective below ~1 keV, simply taking betatron acceleration into account at this lower energy level may cause generation of an excessive number of pancake events compared with the observed change in numbers (Figure 5b). Figure 9a also shows the significant increase in 90° at higher-energy channels above a few tens of keV; this increase may also contribute to the observed increased numbers in pancake events around 60 keV. As to the source of this flux at 90°, particle injection from betatron acceleration associated with increased magnetic field strengths at the dipolarization front, as simulated for high-energy electrons in the tailside may provide a clue to explain it [*Ashour-Abdalla et al*., 2011; *Gabrielse et al*., 2012, 2014; *Birn et al*., 2014]. This mechanism of acceleration was proposed decades ago by *Kivelson et al*. [1973]. High-energy electron populations can also be generated from acceleration by magnetic reconnection at the X line [*Hoshino et al*., 2001], at the magnetic island [*Huang et al*., 2012b], and at the pileup regions of magnetic fields [*Imada et al*., 2007].

Regarding isotropic events, the model-calculated change in the numbers of events after dipolarization (Figure 8c) shows pattern over energies similar to the observed one (Figure 5c). That is to say, both figures exhibit a significant decrease above 1 keV, and the extent of this decrease gradually lessens as energy increases. The model-calculated change in the numbers of butterfly events shows a closer pattern over energies at energy channels above 10 keV. However, for lower energy channels, the model produces excessive numbers of events after dipolarization.

4. Summary and Discussion

Observations by THEMIS probes in Earth's magnetotail in 2008 and 2009 were analyzed to investigate pitch angle distribution features of electrons from a few eV to MeV at 42 dipolarization sites in the inner plasma sheet during geomagnetic activity associated with *AL* index decrease. Changes in the numbers of cigar, pancake, isotropic, and butterfly distribution events after dipolarization were analyzed (Figure 5). Changes in the numbers of cigar and isotropic distribution events after dipolarization were found to be connected. The decrease in the observed number of cigar events below ~1 keV (Figure 5a) is related to greater isotropization of the observed cigar distributions below this energy level. Above ~1 keV, the observed number of cigar events is found to increase distinctly (Figure 5a), which is related to the observations that many isotropic events have evolved into cigar events above this energy level. Therefore, the observed number of isotropic events is found to decrease distinctly above ~1 keV (Figure 5c).

Modeling changes in PAD during dipolarization based on the conservation of the first and second adiabatic invariants have also been used to assess the influence of betatron and Fermi accelerations on PAD. Although previous studies emphasized the significance of Fermi acceleration by field-line shortening for tailside electrons, we find that this may apply only to electrons with energies above 1 keV, as the validity of *J* for each event, depicted by black solid lines, shown in Figure 6. As Figure 8a shows, the greater number of cigar events at energy levels above 1 keV in the model-calculated results is consistent with greater effectiveness of Fermi acceleration above 1 keV. The model-calculated pattern of change in numbers of isotropic events over energies (Figures 8c) is also consistent with the observed pattern (Figure 5c). The above features in the model-calculated results suggest that adiabatic acceleration mechanisms can explain the observed patterns of changes in event numbers over a large range of energies for cigar events and isotropic events.

Nevertheless, other factors to generate more cigar events after dipolarization still need to be considered since the observed changes in the numbers of events are greater than the model-calculated ones, especially at the level of a few keV (Figures 5a and 8a). These factors can be nonadiabatic acceleration mechanisms and external source/loss of flux at specific pitch angles, as addressed in section 3. Observations show that there are events with dominant flux increase in both $\alpha = 0°$ and 180° at lower energies between 200 eV and 10 keV (Figure c) and there are also events with dominant flux decrease at $\alpha = 90°$ from 600 eV to 20 keV (Figure 9b). These observed dominant flux changes in specific pitch angles from external source/loss could contribute to greater numbers of cigar events after dipolarization at the level of a few keV.

As to the pancake events, unlike other three types of PAD, the model-calculated change in the numbers of events after dipolarization is excessive (Figure 8b) than what is shown in observations at most energy channels (Figure 4b). Therefore, the question that the extent to which betatron acceleration could contribute

is important. Nonadiabatic parallel acceleration mechanisms may still be required to interpret the observed increase of cigar events at the level of a few keV; such parallel accelerations could then suppress the effects from betatron acceleration, which could have produced more pancake events in model-calculation results.

Butterfly distributions have been attributed to the effects of shell splitting or magnetopause shadowing as electrons drift [*West et al*., 1973; *Klida and Fritz*, 2013]. Considering the longer time scale of electrons drifting over one orbit, however, this effect should be less important during dipolarization. The formation of butterfly distributions from competition between betatron and Fermi acceleration should be a reasonable hypothesis. However, the model-calculated results show that adiabatic accelerations may still explain the pattern of the observed change in numbers above 10 keV to some degree but not for energy channels below 10 keV (Figures 4d and 8d). Improvements are expected when nonadiabatic acceleration mechanisms are included. Note that before dipolarizations, the numbers of both pancake and butterfly events are much lower than those for cigar and isotropic events (Figure 4). Therefore, finding more pancake events and butterfly events from more observational data would also be helpful to substantiate the conclusions.

In summary, adiabatic accelerations can explain the pattern of changes in the numbers of both cigar and isotropic distribution events over most energy channels up to a few tens of keV. Other factors still need to be considered to explain the observed changes in detail. We hope that the results from the observations/modeling of PAD at dipolarization sites based on adiabatic accelerations presented in this paper motivate future studies.

Acknowledgments

We thank J. Bortnik and S.Y. Fu for their valuable discussions. We are grateful to J. H. Shue and L.H. Lyu of NCU for their assistance. The data in this research are acquired from THEMIS Data Analysis Software (TDAS, now SPEDAS) at the official THEMIS website (http://themis.ssl.berkeley.edu/software.shtml), with which the software can be used to download, open, analyze, and plot scientific data. Thanks to C. Goethel for the instructions on interactive interface of this data analysis software as well as the development team for usage to analyze charged particles. Thanks to K.H. Glassmeier, U. Auster, and W. Baumjohann for the use of FGM data provided under the lead of the Technical University of Braunschweig and with financial support through the German Ministry for Economy and Technology and the German Center for Aviation and Space (DLR) under contract 50 OC 0302. Thanks also to Taiwan AIDA (Ascii and Idl_save Data Archives) maintained by B.S. Lee and W.C. Hsieh at the National Central University. Thanks also to grants and research facilities in ICSWSE at Kyushu University. Also thanks to C.J. Weng and C.C. Chang on the data plots. This research is supported by the facilities of NCU, CHU, and PSSC/NCKU, and from grants 97-NSPO(B)-ST-FA0701, 97-NSPO(B)-SP-FA07-01(C), NSC99-2111-M-006-004-MY3, and NSC102-2111-M-006-002, and NASA grant NNX12AJ57G.

Larry Kepko thanks Jean-André Sauvaud and two other reviewers for their assistance in evaluating this paper.

References

Abel, G. A., A. N. Fazakerley, and A. D. Johnstone (2002), Statistical distributions of field-aligned electron events in the near-equatorial magnetosphere observed by the Low Energy Plasma Analyzer on CRRES, *J. Geophys. Res.*, *107*(A11), 1393, doi:10.1029/2001JA005073.

Angelopoulos, V., C. F. Kennel, F. V. Coroniti, R. Pellat, M. G. Kivelson, R. J. Walker, C. T. Russell, W. Baumjohann, W. C. Feldman, and J. T. Gosling (1994), Statistical characteristics of bursty bulk flow events, *J. Geophys. Res.*, *99*(A11), 21,257–21,280, doi:10.1029/94JA01263.

Angelopoulos, V., et al. (2008), Tail reconnection triggering substorm onset, *Science*, *321*(5891), 931–935, doi:10.1126/science.1160495.

Apatenkov, S. V., et al. (2007), Multi-spacecraft observation of plasma dipolarization/injection in the inner magnetosphere, *Ann. Geophys.*, *25*, 801–814.

Asano, Y., et al. (2010), Electron acceleration signatures in the magnetotail associated with substorms, *J. Geophys. Res.*, *115*, A05215, doi:10.1029/2009JA014587.

Ashour-Abdalla, M., M. El-Alaoui, M. L. Goldsten, M. Zhou, D. Schriver, R. Richard, R. Walker, M. G. Kivelson, and K.-J. Hwang (2011), Observations and simulations of non-local acceleration of electrons in magnetotail magnetic reconnection events, *Nat. Phys.*, doi:10.1038/NPHYS1903.

Åsnes, A., R. W. Friedel, J. Stadsnes, M. Thomsen, N. Østgaard, and T. Cayton (2005), Statistical pitch angle properties of substorm-injected electron clouds and their relation to dawnside energetic electron precipitation, *J. Geophys. Res.*, *110*, A05207, doi:10.1029/2004JA010838.

Auster, H. U., et al. (2008), *Space Sci. Rev.*, *141*(1–4), 235–264, doi:10.1007/s11214-008-9365-9.

Baumjohann, W., M. Hesse, S. Kokubun, T. Mukai, T. Nagai, and A. A. Petrukovich (1999), Substorm dipolarization and recovery, *J. Geophys. Res.*, *104*(A11), 24,995–25,000, doi:10.1029/1999JA900282.

Birn, J., A. Runov, and M. Hesse (2014), Energetic Electrons in Dipolarization Events: Spatial Properties and Anisotropy, *J. Geophys. Res. Space Physics*, *119*, 3604–3616, doi:10.1002/2013JA019738.

Chirikov, B. V. (1987), Particle dynamics in magnetic traps, in *Reviews of Plasma Physics*, vol. 13, edited by B. B. Kadomtsev, 1 pp., Consultants Bureau, New York.

Deng, X., M. Ashour-Abdalla, M. Zhou, R. Walker, M. El-Alaoui, V. Angelopoulos, R. E. Ergun, and D. Schriver (2010), Wave and particle characteristics of earthward electron injections associated with dipolarization fronts, *J. Geophys. Res.*, *115*, A09225, doi:10.1029/2009JA015107.

Elkington, S. R., M. K. Hudson, M. J. Wiltberger, and J. G. Lyon (2002), MHD/particle simulations of radiation belt dynamics, *J. Atmos. Sol. Terr. Phys.*, *64*, 607–615, doi:10.1016/S1364-6826(02)00018-4.

Fu, H. S., Y. V. Khotyaintsev, M. André, and A. Vaivads (2011), Fermi and betatron acceleration of suprathermal electrons behind dipolarization fronts, *Geophys. Res. Lett.*, *38*, L16104, doi:10.1029/2011GL048528.

Fu, H. S., Y. V. Khotyaintsev, A. Vaivads, M. André, and S. Y. Huang (2012a), Electric structure of dipolarization front at sub-proton scale, *Geophys. Res. Lett.*, *39*, L06105, doi:10.1029/2012GL051274.

Fu, H. S., Y. V. Khotyaintsev, A. Vaivads, M. André, V. A. Sergeev, S. Y. Huang, E. A. Kronberg, and P. W. Daly (2012b), Pitch angle distribution of suprathermal electrons behind dipolarization fronts: A statistical overview, *J. Geophys. Res.*, *117*, A12221, doi:10.1029/2012JA018141.

Gabrielse, C., V. Angelopoulos, A. Runov, and D. L. Turner (2012), The effects of transient, localized electric fields on equatorial electron acceleration and transport toward the inner magnetosphere, *J. Geophys. Res.*, *117*, A10213, doi:10.1029/2012JA017873.

Gabrielse, C., V. Angelopoulos, A. Runov, and D. L. Turner (2014), Statistical characteristics of particle injections throughout the equatorial magnetotail, *J. Geophys. Res. Space Physics*, *119*, 2512–2535, doi:10.1002/2013JA019638.

Grigorenko, E. E., R. Koleva, and J.-A. Sauvaud (2012), On the problem of Plasma Sheet Boundary Layer identification from plasma moments in Earth's magnetotail, *Ann. Geophys.*, *30*, 1331–1343, doi:10.5194/angeo-30-1331-2012.

Hada, T., A. Nishida, T. Teresawa, and E. W. Hones Jr. (1981), Bi-Directional Electron Pitch Angle Anisotropy in the Plasma Sheet, *J. Geophys. Res.*, *86*(A13), 11,211–11,224, doi:10.1029/JA086iA13p11211.

Hoshino, M., T. Mukai, T. Terasawa, and I. Shinohara (2001), Suprathermal electron acceleration in magnetic reconnection, *J. Geophys. Res.*, *106*(A11), 25,979–25,997, doi:10.1029/2001JA900052.

Huang, S. Y., M. Zhou, X. H. Deng, Z. G. Yuan, Y. Pang, Q. Wei, W. Su, H. M. Li, and Q. Q. Wang (2012a), Kinetic structure and wave properties associated with sharp dipolarization front observed by Cluster, *Ann. Geophys.*, *30*, 97–107, doi:10.5194/angeo-30-97-2012.

Huang, S. Y., et al. (2012b), Electron acceleration in the reconnection diffusion region: Cluster observations, *Geophys. Res. Lett.*, *39*, L11103, doi:10.1029/2012GL051946.
Imada, S., R. Nakamura, P. W. Daly, M. Hoshino, W. Baumjohann, S. Mühlbachler, A. Balogh, and H. Rème (2007), Energetic electron acceleration in the downstream reconnection outflow region, *J. Geophys. Res.*, *112*, A03202, doi:10.1029/2006JA011847.
Kivelson, M. G., T. A. Farley, and M. P. Aubry (1973), Satellite studies of magnetospheric substorms on August 15, 1968: 5. Energetic electrons, spatial boundaries, and wave-particle interactions at Ogo 5, *J. Geophys. Res.*, *78*(16), 3079–3092, doi:10.1029/JA078i016p03079.
Klida, M. M., and T. A. Fritz (2013), Characterising electron butterfly pitch angle distributions in the magnetosphere through observations and simulations, *Ann. Geophys.*, *31*, 305–314, doi:10.5194/angeo-31-305-2013.
Le Contel, O., et al. (2009), Quasi-parallel whistler mode waves observed by THEMIS during near-earth dipolarizations, *Ann. Geophys.*, *27*, 2259–2275, doi:10.5194/angeo-27-2259-2009.
Runov, A., V. Angelopoulos, X.-Z. Zhou, X.-J. Zhang, S. Li, F. Plaschke, and J. Bonnell (2011), A THEMIS multicase study of dipolarization fronts in the magnetotail plasma sheet, *J. Geophys. Res.*, *116*, A05216, doi:10.1029/2010JA016316.
Runov, A., V. Angelopoulos, C. Gabrielse, X.-Z. Zhou, D. Turner, and F. Plaschke (2013), Electron fluxes and pitch-angle distributions at dipolarization fronts: THEMIS multipoint observations, *J. Geophys. Res Space Physics.*, *118*, 744–755, doi:10.1002/jgra.50121.
Sergeev, V. A., W. Baumjohann, and K. Shiokawa (2001), Bi-directional electron distributions associated with near-tail flux transport, *Geophys. Res. Lett.*, *28*(19), 3813–3816, doi:10.1029/2001GL013334.
Shiokawa, K., W. Baumjohann, and G. Paschmann (2003), Bi-directional electrons in the near-Earth plasma sheet, *Ann. Geophys.*, *21*, 1497.
Sigsbee, K., Slavin, J. A., Lepping, R. P., Szabo, A., Ã¯eroset, M., Kaiser, M. L., Reiner, M. J., and Singer, H. J. (2005), Statistical and superposed epoch study of dipolarization events using data from Wind perigee passes, *Ann. Geophys.*, *23*, 831–851.
Smets, R., D. Delcourt, J. A. Sauvaud, and P. Koperski (1999), Electron pitch angle distributions following the dipolarization phase of a substorm: Interball-Tail observations and modeling, *J. Geophys. Res.*, *104*(A7), 14,571–14,581, doi:10.1029/1998JA900162.
Walt, M. (2005), *Introduction to Geomagnetically Trapped Radiation*, Cambridge Univ. Press, New York.
Wang, R., Q. Lu, C. Huang, and S. Wang (2010), Multispacecraft observation of electron pitch angle distributions in magnetotail reconnection, *J. Geophys. Res.*, *115*, A01209, doi:10.1029/2009JA014553.
West, H. I., Jr., R. M. Buck, and J. R. Walton (1973), Electron pitch angle distributions throughout the magnetosphere as observed on Ogo 5, *J. Geophys. Res.*, *78*(7), 1064–1081, doi:10.1029/JA078i007p01064.
Wu, P., T. A. Fritz, B. Larvaud, and E. Lucek (2006), Substorm associated magnetotail energetic electrons pitch angle evolutions and flow reversals: Cluster observation, *Geophys. Res. Lett.*, *33*, L17101, doi:10.1029/2006GL028297.
Zheng, H., S. Y. Fu, Q. G. Zone, Z. Y. Pu, Y. F. Wang, and G. J. Parks (2012), Observations of ionospheric electron beams in the plasma sheet, *Phys. Rev. Lett.*, *109*, 205001, doi:10.1103/PhysRevLett.109.205001.